

A second view on the X-ray polarization of NGC 4151 with IXPE

V. E. Gianolli,^{1,2,*} S. Bianchi,² E. Kammoun,² A. Gnarini,² A. Marinucci,³ F. Ursini,² M. Parra,^{1,2} A. Tortosa,⁴ A. De Rosa,⁵ D. E. Kim,^{5,6,7} F. Marin,⁸ G. Matt,² R. Serafinelli,⁴ P. Soffitta,⁵ D. Tagliacozzo,² L. Di Gesu,³ C. Done,^{9,10} H. L. Marshall,¹¹ R. Middei,^{5,12} R. Mikusincova,⁵ P-O. Petrucci,¹ S. Ravi,¹¹ J. Svoboda,¹³ F. Tombesi,^{7,14,15}

Affiliations are shown at the end of the paper

Received XXX; accepted YYY

ABSTRACT

We report on the second observing program of the active galactic nucleus NGC 4151 with simultaneous Imaging X-ray Polarimetry Explorer (*IXPE*; 750 ks), *NuSTAR* (~ 60 ks), *XMM-Newton* (~75 ks), and *NICER* (~65 ks) pointings. NGC 4151 is the first Type-1 radio-quiet Seyfert galaxy with constrained polarization properties for the X-ray corona. Despite the lower flux state in which the source is re-observed and the resulting higher contribution of the constant reflection component in the *IXPE* energy band, our results are in agreement with the first detection. From the polarimetric analysis, a polarization degree $\Pi = 4.7 \pm 1.3$ per cent and angle $\Psi = 77^\circ \pm 8^\circ$ east of north (68 per cent confidence level) are derived in the 2.0 – 8.0 keV energy range. Combining the two observations leads to polarization properties that are more constrained than those of the individual detections, showing $\Pi = 4.5 \pm 0.9$ per cent and $\Psi = 81^\circ \pm 6^\circ$ (with detection significance $\sim 4.6\sigma$). The observed polarization angle aligns very well with the radio emission in this source, supporting, together with the significant polarization degree, a slab or wedge geometry for the X-ray corona. However, a switch in the polarization angle at low energies ($37^\circ \pm 7^\circ$ in the 2-3.5 keV bin) suggests the presence of another component. When it is included in the spectro-polarimetric fit, a high polarization degree disfavors an interpretation in terms of a leakage through the absorbers, rather pointing to scattering from some kind of mirror.

Key words. polarization – X-rays: galaxies – X-rays: individuals: NGC 4151 – galaxies: active – galaxies: Seyfert

1. Introduction

X-ray polarimetry has emerged as a powerful tool in unveiling the geometry of one of the innermost and most enigmatic regions of active galactic nuclei (AGN): the X-ray corona. According to the Unified Model of AGN, the corona is composed of hot (with a typical temperature of $kT_e \simeq 10 - 100$ keV, e.g., Fabian et al. 2015, 2017; Tortosa et al. 2018) and rarefied optically thin electron plasma situated in the innermost region of the accretion flow. This region up-scatters the UV photons emitted by the disk, producing the primary X-ray emission (Sunyaev & Titarchuk 1980; Zdziarski et al. 2000). The polarization signal of the coronal emission is very sensitive to the geometry of the scattering material (e.g., Schnittman & Krolik 2010; Tamborra et al. 2018; Zhang et al. 2019; Marinucci et al. 2022; Ursini et al. 2022; Gianolli et al. 2023; Ingram et al. 2023; Tagliacozzo et al. 2023). In the past, multiple studies on the physical properties of the X-ray corona (i.e., the optical depth τ and the electron temperature kT_e , Shapiro et al. 1976) have been performed (e.g., Petrucci et al. 2001; Matt et al. 2015; Ricci et al. 2018; Tortosa et al. 2018; Kamraj et al. 2022; Kang & Wang 2022; Serafinelli et al. 2024, and references therein). However, only with the launch of the Imaging X-ray Polarimeter Explorer (*IXPE*, Weisskopf et al. 2022) mission and with its synergy together with simultaneous observations of *NuSTAR* and *XMM-Newton*, new insights have been obtained on the geometry of this region in type-1 AGN (Gianolli et al. 2024; Marin et al. 2024).

NGC 4151 is one of the X-ray brightest Seyfert galaxies in the local Universe. Intensively studied, it shows different layers

of absorption, from both neutral and ionized gas (e.g., Beuchert et al. 2017; Gianolli et al. 2023). Archival observations of the source reveal significant spectral variability in the 1 – 6 keV range. Furthermore, the source shows transitions from optical type 1.5 during high-flux states, where the AGN can reach a flux level as high as $F_{0.5-10\text{keV}} \sim 2.8 \times 10^{-10}$ erg s⁻¹ cm⁻², to optical type 1.8 during low-flux states ($F_{0.5-10\text{keV}} \sim 8.7 \times 10^{-11}$ erg s⁻¹ cm⁻²; see Antonucci & Cohen 1983; Shapovalova et al. 2012; Beuchert et al. 2017).

NGC 4151 is the first Type-1 radio-quiet AGN with constrained polarization properties for the X-ray corona. From the polarimetric analysis, a polarization degree (PD) of $\Pi = 4.9 \pm 1.1$ per cent (68 per cent confidence level) and a polarization angle (PA) of $\Psi = 86^\circ \pm 7^\circ$ have been measured with a significance above 99.99 per cent (Gianolli et al. 2023, “G23” hereafter). Given that the primary X-ray emission was the dominant component in the *IXPE* energy band and the reflection, arising from the reprocessing of the primary continuum off surrounding material (such as the torus), contributed only up to 6 per cent, the observed PD and PA refer to the primary continuum. When taken into account in the spectro-polarimetric analysis, and setting the primary continuum and reflection PAs to differ by 90 degrees, a PD = 7.7 ± 1.5 per cent and PA = $87^\circ \pm 6^\circ$ for the X-ray primary emission are found. Numerical simulations in G23 show that, based on the observed X-ray polarization properties, a radially-extended slab geometry is preferred for the corona. Interestingly, a further component with different polarization properties may be the cause of the observed change in polarization properties in the 2-3.5 keV band (PD = 4.3 ± 1.6 per cent and PA = $42^\circ \pm 11^\circ$). Due to its high variability in the X-ray band, NGC 4151

* E-mail: vittoria.gianolli@univ-grenoble-alpes.fr

is an excellent candidate for studying potential changes in the observed polarization properties.

In the following, we present the spectral and spectropolarimetric analyses of the simultaneous *IXPE*, *NuSTAR*, and *XMM-Newton* data and the results of the *NICER* monitoring. The structure of this paper is as follows. Sect. 2, we provide details on the observations and data reduction processes for *IXPE*, *XMM-Newton*, *NuSTAR*, and *NICER*. Sect. 3, we present the findings of the polarimetric, spectral, and spectropolarimetric analyses. In Sect. 4 the results are discussed.

2. Observing campaign and data reduction

The second *IXPE* observation of NGC 4151 was performed during the 1st Cycle of the *IXPE* General Observer program¹. Due to the long exposure time (750 ks), it has been divided into two segments: 23rd to 28th April and 15th to 26th May 2024. We used the level 2 event files, which are calibrated adopting a standard *IXPE* pipeline from the Science Operation Center (SOC)². We apply the background rejection method following Di Marco et al. (2023)’s guidelines for faint sources. To extract the source (background) data in the three detector units (DUs), a 68'' circle (annulus with internal radius of 180'' and outer of 240'') was adopted. The source extraction radius was derived iteratively to maximize the signal-to-noise ratio in the 2.0 – 8.0 keV band, similar to the procedure described in Piconcelli et al. (2004). Any remaining background contribution is subtracted during the polarimetric analysis. Subsequently, to estimate the polarization properties, we employ two methods: (1) creating the polarization cube (PCUBE; using the *IXPEOBSSIM* software version 31.0.1; Baldini et al. 2022), and (2) generating *I*, *Q*, and *U* spectra using *xselect* (from the *HEASOFT* package version 6.33.2; NASA Heasarc 2014) considering the weighted analysis method with the parameters `stokes=Neff` (Di Marco et al. 2022). Both methods adopt the latest available calibration file, i.e. version 13 (20240101) in *IXPEOBSSIM* and CALDB 20240125 for *xselect*. The Ancillary Response File (ARF) and Modulation Response File (MRF) for each detector unit are generated using the *ixpecalcarf* task and considering the same extraction radius used for the source region.

To constrain the physical properties of the X-ray corona and disentangle the contribution of each spectral component, we requested simultaneous *NuSTAR* and *XMM-Newton* observations. However, due to a *NuSTAR* star tracker blockage for the target and other time-constrained *NuSTAR* and *XMM* observations during the second window of the scheduled *IXPE* observation, both observations have been divided into two pointings.

XMM-Newton observed NGC 4151 on May 21st–22nd (“X1” hereafter) and on May 24th–25th (“X2” hereafter), 2024 for 14 ks and 25 ks (effective exposure times after filtering process) of exposure time using the EPIC pn (Strüder et al. 2001). For both observations, the source and background spectra were extracted following G23 extraction radii. A correction for effective area was applied using the SAS keyword, `APPLYABSFLUXCORR`, specifically designed to improve consistency with simultaneous *NuSTAR* data.

The *NuSTAR* (Harrison et al. 2013) observations have been carried out from May 22nd to 23rd (“N1” hereafter) and from May 25th to 27th (“N2” hereafter), 2024, adopting both

coaligned X-ray telescopes equipped with Focal Plane Module A (FPMA) and B (FPMB). The *Nupipeline* task was employed alongside the latest calibration files from the database (CALDB 20221229) to generate and calibrate cleaned event files. Extraction radii for source and background were set as those adopted by G23, i.e. 2' and 1.22', respectively. The net exposure times for FPMA and FPMB during N1 resulted to be 25 and 24 ks, while for N2 are 34 and 33 ks. As found in the previous campaign, significant deviations from the pn spectrum are still present in the *NuSTAR* spectra below 4 keV. Hence, *NuSTAR* data will be considered only above 4 keV (see e.g., G23). We account for an energy shift of around 2000 km s⁻¹ at the iron line using *vashift* to address lingering calibration issues, which have also been observed in the past (Gianolli et al. 2023; Ingram et al. 2023; Serafinelli et al. 2023).

Given that the coverage of *XMM* and *NuSTAR* observations is limited to the second *IXPE* observing window and due to the highly variable nature of NGC 4151, it is essential to track its absorption/flux state also during the first segment. Hence, we requested a daily monitoring of the source with the Neutron Star Interior Composition Explorer (*NICER*, Gendreau et al. 2012; Arzoumanian et al. 2014; Gendreau et al. 2016) from April 22 to April 30, 2024 for a total of ~35 ks. *NICER* data were also collected between May 1st and 14th (other ~30 ks), allowing us to check for any changes during the time-frame between each *IXPE* pointing.

The *NICER* unfiltered data events were reprocessed using the *nicer12* tool included in the *HEASOFT* software package using the latest software and calibration files (27/02/2024). We applied the *nicer13-spect* task to the clean event files to obtain the spectra. For the background we used the *SCORPEON* model, which includes contributions from many physically-motivated components. It takes into account sky-related components such as the cosmic X-ray background, local hot bubble and galactic halo, and also non X-ray background components such as cosmic rays, South Atlantic Anomaly, trapped electrons, precipitating electrons, and low energy storm-related electrons.

The extracted spectra have been binned following Kaastra & Bleeker (2016) method. All uncertainties are provided at a 68 per cent (1 σ) c.l., unless otherwise specified, and upper/lower limits are reported at a 99 per cent (2.6 σ) c.l. for one single parameter. Throughout our analysis, we consider a redshift of $z = 0.003326$ (Wolfinger et al. 2013), along with cosmological parameters $H_0 = 70$ km s⁻¹ Mpc⁻¹, $\Lambda_0 = 0.73$ and $\Lambda_m = 0.27$.

3. Data analysis

3.1. *IXPE* polarimetric analysis

We report the results of the unweighted PCUBE analysis on the second *IXPE* observation of NGC 4151. For the two segments separately, we obtain in the 2–8 keV energy band (from the three combined DUs), after background subtraction, only an upper limit for the polarization degree (i.e., $\Pi < 7.8$ per cent) in the first, and a significant detection (with $\Pi = 5.4 \pm 1.6$ per cent and polarization angle $\Psi = 78^\circ \pm 8^\circ$) in the second. Given the consistency of the PDs in the two segments, we proceed by summing them together, finding $\Pi = 4.7 \pm 1.3$ per cent and $\Psi = 77^\circ \pm 8^\circ$, with a detection significance at 99.84 per cent confidence level ($\sim 3.2\sigma$). In Table 1 (middle part), we show the Π and Ψ obtained in the 3 energy bands adopted in G23: 2.0 – 3.5, 3.5 – 5.0, and 5.0 – 8.0 keV. However, we found only for the last energy bin a significant detection (at $\sim 3.3\sigma$) and marginal detections for the first and middle bins (at $\sim 2.6\sigma$ and $\sim 1.2\sigma$, respectively).

¹ https://heasarc.gsfc.nasa.gov/docs/ixpe/proposals/aol/c1_targets.html

² <https://heasarc.gsfc.nasa.gov/docs/ixpe/analysis/IXPE-SOC-DOC-009-UserGuide-Software.pdf>

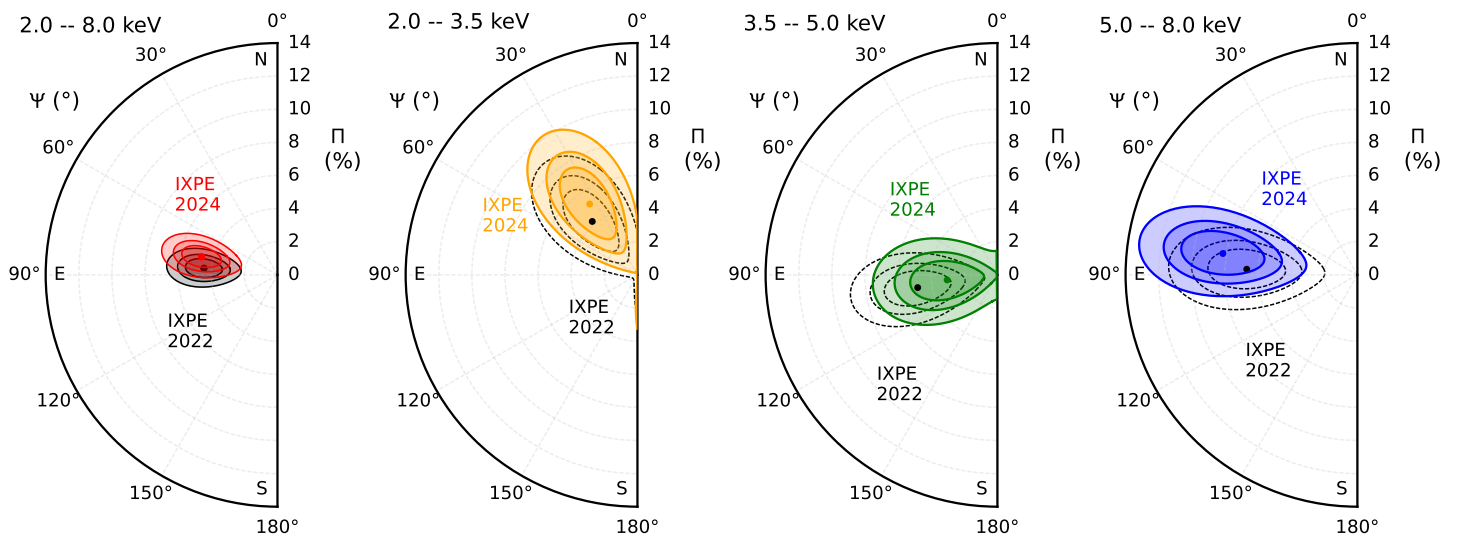


Fig. 1. Comparison between first and second *IXPE* observations. Polarization contours (68, 90, and 99 per cent confidence levels; see eq. 32 of [Muleri 2022](#)) for the polarization degree Π and the polarization angle Ψ with respect to the north direction. First left panel: comparison between first (in black) and second (in red) observation considering *IXPE* full energy band. Second to fourth panels: comparison between first and second observation considering the division in three energy bins. Colors refer to the 2.0 – 3.5 keV (black the first and yellow the second observation), 3.5 – 5.0 keV (black the first and green the second observation), and 5.0 – 8.0 keV (black the first and blue the second observation) energy ranges, respectively.

To compare the results of the second observation with those of the first, we have also re-extracted the PCUBE of the latter, adopting the new calibration files available in *IXPE*OBSIM. We report the derived polarization properties in Table 1, upper part. In Figure 1, left panel, we present the comparison between the polarization contours of the first and second detections in the full energy band of *IXPE*. Meanwhile, in the right panels of Figure 1, we show the polarization contours obtained for the three energy bins in the first and second observations. We observe that the polarization properties of the second observation (for both the 2.0 – 8.0 keV energy band and the individual bins) are always well consistent with those found during the first detection. Hence, we combined the PCUBE of both observations. In Fig. 2, we report the contours of the polarimetric properties obtained in the full energy band and for the three bins. We observe that, once the two observations are combined together, all PDs and PAs are more constrained than in the individual observations. Particularly, for the full energy band of *IXPE* we obtain $\Pi = 4.5 \pm 0.9$ per cent and $\Psi = 81^\circ \pm 6^\circ$ (with detection significance $\sim 4.6\sigma$). For the three energy bins, we present in Table 1 the polarization degrees, now significantly detected (at $\sim 3.5\sigma$, $\sim 3.3\sigma$, and $\sim 4.5\sigma$, respectively) in each energy bin, and the polarization angles. In both the second and combined observations, the peculiar behavior detected by [G23](#) in the 2.0 – 3.5 keV energy bin remains evident and a difference of $\sim 45^\circ$ between the PA in this bin and that derived for the full band is present. Meanwhile, a difference of $\sim 60^\circ$ is observed between the polarization angles of the 2.0–3.5 keV and 3.5–5.0 keV energy bins.

3.2. Spectral Analysis: XMM-Newton, NuSTAR, and NICER

To perform the spectral analysis of NGC 4151, we use *XSPEC* version 12.13.0 ([Arnaud 1996](#)), considering the 0.5 – 10.0 keV *XMM-Newton* and 4.0 – 79.0 keV *NuSTAR* spectra simultaneously. The source is detected in an average flux state, with $F_{0.5-10 \text{ keV}} = 1.07(1.33) \times 10^{-10} \text{ erg s}^{-1} \text{ cm}^{-2}$ for X1+N1

Table 1. Polarization parameters of the first, second and the combination of the two *IXPE* observations for different energy bands.

Obs	Energy range [keV]	$\Pi \pm 1\sigma$ [%]	$\Psi \pm 1\sigma$ [deg]
1st	2.0 – 8.0	4.6 ± 1.2	85 ± 8
	2.0 – 3.5	4.2 ± 1.6	40 ± 11
	3.5 – 5.0	4.9 ± 1.4	99 ± 8
	5.0 – 8.0	6.7 ± 2.0	87 ± 9
2nd	2.0 – 8.0	4.7 ± 1.3	77 ± 8
	2.0 – 3.5	5.2 ± 1.7	34 ± 10
	3.5 – 5.0	3.1 ± 1.5	96 ± 14
	5.0 – 8.0	8.2 ± 2.2	81 ± 8
Combined	2.0 – 8.0	4.5 ± 0.9	81 ± 6
	2.0 – 3.5	4.6 ± 1.1	37 ± 7
	3.5 – 5.0	4.0 ± 1.0	98 ± 7
	5.0 – 8.0	7.2 ± 1.4	84 ± 6

(X2+N2), lower than the first campaign ($F_{0.5-10 \text{ keV}} = 1.73 \times 10^{-10} \text{ erg s}^{-1} \text{ cm}^{-2}$). We show in Fig. 3 the *XMM* and *NuSTAR* spectra of the first and second observational campaigns. The spectra appear consistent below 1 keV and exhibit a similar spectral shape at high energies. Most of the spectral variability is concentrated between 2.0 and 6.0 keV, suggesting variability in obscuration. Hence, given the complexity of modeling the X-ray spectrum of NGC 4151 (e.g.,

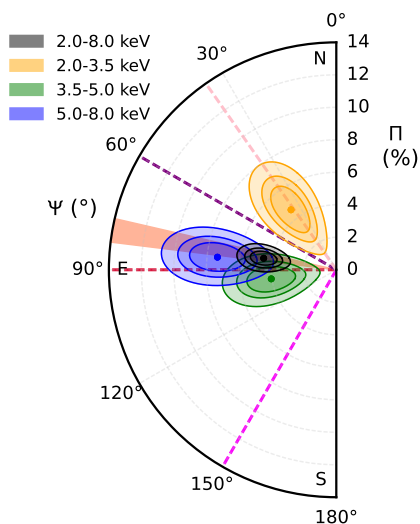


Fig. 2. Combined 1st and 2nd *IXPE* observations. Polarization contours (68, 90, and 99 per cent confidence levels) for the polarization degree Π and the polarization angle Ψ with respect to the north direction. Colors refer to the 2.0 – 8.0 keV (in black), 2.0 – 3.5 keV (in yellow), 3.5 – 5.0 keV (in green), and 5.0 – 8.0 keV (in blue) energy ranges, respectively. The orange region shows the direction of the radio emission. The red, purple, and pink dashed lines represent the direction of the inner few pc of the radio jet, NLR, and of an unclassified feature, respectively (see Sect. 4). The magenta dashed line shows the direction of the torus, which has been identified in X-rays with a position angle of $\sim 150^\circ$ (Wang et al. 2011), appearing to coincide with the H_2 region identified by Storchi-Bergmann et al. (2009). It is worth noting that the accretion disk axis could be misaligned with the torus by $\sim 20^\circ$ (May et al. 2020). Furthermore, Bentz et al. (2022) describe the BLR as a thick disk with $\sim 57^\circ$ opening angle and $\sim 58^\circ$ inclination angle, suggesting our view skims just above the BLR surface.

Weaver et al. 1994; Zdziarski et al. 1996; Yang et al. 2001; De Rosa et al. 2007; Kraemer et al. 2008; Lubiński et al. 2010; Gianoli et al. 2023), we adopt the same model used in G23: (tbabs)*(CLOUDY + zgauss + PC*PC*WA*(BORUS 1 + BORUS 2 + nthcomp)). tbabs models the Galactic absorption, a thermally Comptonized continuum (nthcomp; Zdziarski et al. 1996; Życki et al. 1999) represents the primary X-ray emission, and BORUS (Baloković et al. 2018, 2019) is used for modeling the reflection component. Following G23 approach, we separate the reflection component (i.e., the emission reprocessed by a torus) from the fluorescent lines by using specific BORUS tables. Soft X-ray emission is accounted for by incorporating a photoionized plasma emission component generated with CLOUDY (Ferland et al. 1998; Bianchi et al. 2010) and the residuals around the O VII emission line triplet are mitigated using a Gaussian line. The different layers of absorption (e.g., Keck et al. 2015; Gianoli et al. 2023) are modeled by two neutral partial-coverers (PC, zpcfabs), along with a warm absorber (WA, modeled with zxipcf and covering factor fixed to 1). The applied multiplicative constants (which accommodate cross-calibration uncertainties between FPM modules and EPIC pn, and marginal flux variability of the source as the observations are not strictly simultaneous) are of the order of 1.20.

As a first step, we analyzed the Fe $K\alpha$ emission line by focusing on the 5.0 – 10.0 keV energy band. By doing so, we aim at assessing the possible presence of a significant relativistic reflection component and variability of the line. As found by G23 for the first campaign, NGC 4151 does not show a clear relativistic component in the new data, differently from what found in some

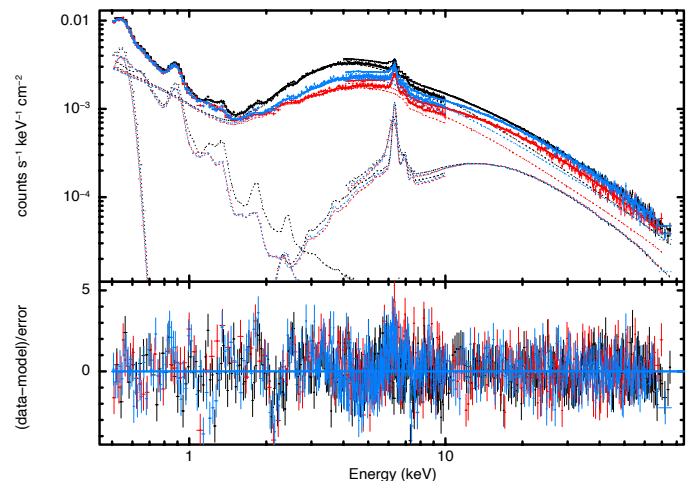


Fig. 3. XMM-*Newton* and *NuSTAR* spectra with residuals. In black the XMM-*Newton*/EPIC pn and the grouped *NuSTAR* FPMA and FPMB of the first campaign are shown. In red, the XMM-*Newton*/EPIC pn and the grouped *NuSTAR* FPMA and FPMB of the second campaign (first segments) are shown. In blue, the XMM-*Newton*/EPIC pn and the grouped *NuSTAR* FPMA and FPMB of the second campaign (second segments) are presented.

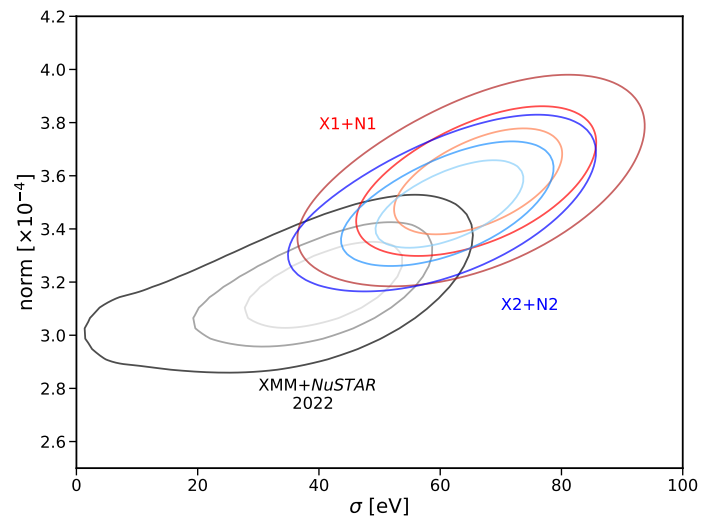


Fig. 4. Iron emission line: width vs normalization contour plots. Black refers to the 2022 data, red to the X1+N1 data and blue to the X2+N2 data.

previous observations of the source (e.g., Yaqoob et al. 1995; Zoghbi et al. 2019, and references therein). The line can be modeled with a single Gaussian, only slightly resolved ($\sigma \sim 60 - 70$ eV). We find no evidence of variability in line parameters (intensity and width) either between X1+N1 and X2+N2, or with respect to the first campaign (Fig. 4). Consequently, the equivalent width of the iron line anti-correlates with the flux of the source, being $EW = 150 \pm 15$ (126_{-7}^{+10}) eV in the X1+N1 (X2+N2) data, and $EW = 100 \pm 6$ eV in the 2022 data.

Subsequently, we consider the full broad-band X1+N1 and X2+N2 data, and we fit them together with the XMM+*NuSTAR* data from the 1st campaign to identify any variability in the spectral components. We assume that the reflection component did

not change, as evidenced by the absence of variation in the Fe $K\alpha$ emission line. Meanwhile, we allow the photon index and the normalization of the primary continuum to vary. Furthermore, all absorbers (both neutral and ionized) show a significant variation between X1+N1 and the 2022 campaign, with only the first neutral PC (column density and covering factor) differing between X1+N1 and X2+N2 (see Table 2). A small, but significant change is also observed for the parameters of the photoionized gas that models the soft X-ray emission, confirming a similar variability noted by Zoghbi et al. (2019). In the end, we obtain an acceptable best-fit with $\chi^2/\text{d.o.f} = 5878/5208$. We show the best-fit parameters in Table 2 (those of the 2022 campaign are also reported), and the spectra with residuals in Fig. 3.

Whereas in G23 the reflection (reprocessed continuum and fluorescent lines) contribution was only about 6 per cent in the 2–8 keV energy band, we now find it to be 26 per cent for X1+N1 and 21 per cent for X2+N2. The contribution of the Fe $K\alpha$ line is 8 (7) per cent in the 5.0 – 8.0 keV for the two new observations. We note that the observed trend, i.e. as flux increases (from X1+N1 to X2+N2 and up to the 2022 level) the contribution of the reflection is decreasing, is in agreement with our assumption on the constant reflection (which is justified via the iron line). Moreover, as also obtained in G23, the contribution of the photoionized emission in the 2–3.5 keV band is not significant and becomes so only at lower energies. On the other hand, the 2–3.5 keV band manifests an excess relative to the absorbed primary continuum, which has been interpreted in this model as the primary emission leakage through the partial coverers. Its contribution is around 15 (22) per cent in the X1+N1 (X2+N2) observation, becoming 7 (8) per cent for X1+N1 (X2+N2) in the 3.5 – 5.0 keV, and 2 (3) per cent for X1+N1 (X2+N2) in the 5.0 – 8.0 keV bin.

A total of 23 *NICER* observations were also performed continuously from the beginning of the first segment of *IXPE* until the beginning of the second. In Fig. 5, we report the variation of the 2.0 – 10.0 keV flux compared to the values observed during the past and new *XMM+NuSTAR+IXPE* campaigns. We note that the 6 observations strictly simultaneous to the first segment of the new *IXPE* observation (see light green band on the left of Fig. 5), display a flux similar to that measured during X2+N2. We thus fit the 6 simultaneous pointings to monitor possible changes in the absorbers and continuum. We note that, due to discrepancies between the *NICER* and *XMM* spectra below 1 keV, and because this energy band is not crucial for our purposes, we only consider data above this energy. A good fit ($\chi^2/\text{d.o.f} = 718/612$) is obtained allowing the normalization of the primary emission and the first neutral PC (column density and covering factor) to vary for the different spectra. In Fig. 6, we report the variation observed for the three free parameters.

In conclusion, from the *NICER* analysis, we confirm the presence of neutral variable absorption along the line-of-sight on short (~ 1 day) timescales during the first and between each segment of the *IXPE* observation. The same variability, along with that of the X-ray photon index, is also evident when fitting *XMM* and *NuSTAR* data. This variability extends over long timescales. Indeed, the parameters of the continuum and absorbers show variation when compared to the data taken in 2022 (see Table 2). However, the overall adopted model appears to remain valid. Therefore, in the spectro-polarimetric analysis discussed in the next section, we will use this model for the two *IXPE* campaigns, allowing these parameters to vary.

3.3. Spectro-polarimetric analysis: *XMM-Newton*, *NuSTAR* and *IXPE*

The spectro-polarimetric analysis has been conducted following the methodology presented in G23: i) we fit the *IXPE* data (I , Q and U spectra of the three detectors, for both observations, see Fig. 7) by applying the *XMM-Newton+NuSTAR* best-fit (see Sec. 3.2). We include inter-calibration constant (which are free to vary and of the order of ~ 1.00) between each detector. Given the variability reported in Sect. 3.2, we leave to vary the primary continuum normalization and the parameters of the first neutral partial covering for the second observation (in comparison to those of the first observation that are set to the best-fit values derived in G23). Sect. 3.1. ii) *polconst* multiplicative models are added to derive the polarization of each individual component. PD and PA are set to 0 for the *BORUS* and *CLOUDY* component (see G23). We note that G23 spectro-polarimetric model considers a further spectral component with assigned *polconst*: the primary continuum leaking through the absorbers. By adopting the same configuration reported in the first paper (i.e., with the primary continuum and the reflection PAs forced to differ by 90° and PDs free to vary, while the PD and PA of the leaking emission are set to 0), we obtain a good fit ($\chi^2/\text{d.o.f} = 1298/1222$ for the 18 *IXPE* spectra) in which the polarization is attributed to the primary continuum, with $\Pi = 7.1 \pm 1.2$ per cent and $\Psi = 84^\circ \pm 5^\circ$. Only an upper limit is derived for the reflection component $\Pi < 17$ per cent (Model 1 in Table 3). As in G23, if the continuum and reflection PAs are set to be parallel (i.e., given a slab coronal geometry, the reflection is from the disk), the reflection component PD is unconstrained.

Despite the goodness of the above fit, an excess below 4 keV in the Q and U spectra is clearly visible (see Fig. 7, right panel). This excess drives the change in polarization angle in the 2 – 3.5 keV energy bin (see Sect. 3.1). Given the higher statistic from considering both observations, we attempt to simultaneously constrain the polarization properties of the leaking emission, along with those of the X-ray continuum and of the reflection. Starting from the above spectro-polarimetric fit, we now allow PA and PD of the leakage to vary. Since we are unable to constrain also the polarimetric properties of the reflection component, we assume it is either unpolarized or has PD = 20%, with a PA parallel or perpendicular to that of the primary continuum (see Table 3, Model 2 and Model 3). The statistical quality of the fit improves (down to $\chi^2/\text{d.o.f} = 1272/1221$), with PD in the range $\sim 10 - 20\%$ for both the primary continuum and the soft component in all cases, and polarization angles of ~ 100 and $\sim 20^\circ$, respectively.

We show in Fig. 8 the PD and PA as a function of energy, as predicted by the models described above and compared to the observed values, re-binned at 1 keV and grouped (all detectors for both observations) for a better visualization. Although these fits account for the switch of PA in the soft X-rays, their physical interpretation is problematic. A PD of around 14 per cent for the soft component may suggest that what we observe is not a leakage through the absorbing layers, but rather the reflection of the primary emission on the inner accretion flow or on a mirror close to the disk. However, a Comptonizing X-ray corona cannot produce a PD in the 16–20 per cent range. For instance, a slab corona, which produces the highest polarization degrees, can reach up to PD ~ 12 per cent, depending on the inclination (see Ursini et al. 2022).

In order to disentangle the coronal emission from the soft component, we test a simplified phenomenological model, composed only by a power-law and a black-body (with temperature \sim

Table 2. Best-fit from the spectral analysis.

Parameter	Value 1st obs	Value X1+N1	Value X2+N2
CLOUDY (Photoionized emitter)			
$\log U$	1.35 ± 0.01		$1.11^{+0.01}_{-0.02} +$
$\log(N_{\text{H}} / \text{cm}^{-2})$	21.63 ± 0.02		$21.54^{+0.01}_{-0.02} +$
PC 1 (Neutral absorber 1)			
$\log(N_{\text{H}} / \text{cm}^{-2})$	23.02 ± 0.01	23.27 ± 0.01	23.18 ± 0.01
Cf	0.78 ± 0.01	0.73 ± 0.01	0.75 ± 0.01
PC 2 (Neutral absorber 2)			
$\log(N_{\text{H}} / \text{cm}^{-2})$	22.64 ± 0.01		$22.68 \pm 0.01 +$
Cf	0.95 ± 0.01		$0.93 \pm 0.01 +$
WA (Warm absorber)			
$\log(N_{\text{H}} / \text{cm}^{-2})$	23.13 ± 0.03		$23.59^{+0.04}_{-0.05} +$
$\log(\xi / \text{erg cm s}^{-1})$	4.12 ± 0.02		$4.31 \pm 0.03 +$
BORUS 1/2 (Neutral reflector 1/2)			
$\log(N_{\text{H}} / \text{cm}^{-2})$	24.45 ± 0.01		24.45^*
$A_{\text{Fe}}/A_{\text{Fe},\odot}$	0.62 ± 0.01		0.62^*
norm	0.09 ± 0.01		0.09^*
nthcomp (Comptonized primary continuum)			
Γ	1.85 ± 0.01	1.88 ± 0.01	1.82 ± 0.01
kT_e [keV]	60^{+7}_{-6}		60^*
norm	0.093 ± 0.001	0.067 ± 0.002	0.071 ± 0.001
$\chi^2/\text{d.o.f.}$	743/660	2556/2245	2576/2255
$F_{2-10 \text{ keV}} / [\times 10^{-10} \text{ erg cm}^{-2} \text{ s}^{-1}]$	1.680 ± 0.003	1.025 ± 0.004	1.277 ± 0.004
$L_{2-10 \text{ keV}} / [\times 10^{42} \text{ erg s}^{-1}]$	4.060 ± 0.006	2.477 ± 0.010	3.085 ± 0.009

Notes.

*: during X1+N1 and X2+N2 data fitting, we fix these values to those obtained in G23 best-fit (we report for the first observation the uncertainties obtained in G23).

+: during data fitting, we fix the values of X2+N2 to those obtained for X1+N1, as they do not vary when left free.

Normalization in units of photons $\text{s}^{-1} \text{cm}^{-2} \text{keV}^{-1}$.

The best-fit values are adopted in the spectro-polarimetric analysis.

0.5 keV), each obscured by a different layer of neutral matter (of the order of 10^{23} and 10^{22} cm^{-2} , respectively). The two components have separate polarization properties, while the Fe $K\alpha$ line is considered as unpolarized. From a statistical point of view, the fit is similar to the previous ones ($\chi^2/\text{d.o.f.} = 1287/1224$). While still reproducing the angle switch at low energies, this model recovers a PD $\sim 7\%$ for the primary emission, with a similar PD ($\sim 8\%$) for the soft component (Table 3, Model 4, and Fig. 8).

4. Discussion and conclusions

The spectral analysis of the available XMM-Newton, NuSTAR, and NICER data of NGC 4151 (see Sect. 3.2) reveals variations in the absorbers and in the primary continuum compared to the 2022 data and between the two new sets of observations. Specifically, we observe variability in the X-ray photon index, continuum normalization, and both neutral and ionized absorbers along the line-of-sight on short (~ 1 day) and long (~ 1.5 year) timescales, suggesting ongoing dynamic processes in the source environment (see Fig. 5 and 6, and Table 2). Meanwhile, all the physical parameters of the reflection component are compatible

with being constant with respect to the past data (see Table 2 and Fig. 4), so its contribution to the IXPE energy band is higher in the new observations (see Table 2).

Despite the lower flux state of NGC 4151 and the higher contribution of the reflection component, we find no evidence for variations in the observed polarization properties, with polarization degree (PD) and polarization angle (PA) being in good agreement between the first and second observations in all considered energy ranges (see polarimetric analysis in Sect. 3.1). This allows for an analysis of the combined observations, which yields better constraints for PD and PA. In particular, in the full IXPE energy band (i.e., 2.0 – 8.0 keV), we obtain $\Pi = 4.5 \pm 0.9$ per cent and $\Psi = 81^\circ \pm 6^\circ$. The latter aligns very well with the radio emission (see Fig. 2), which shows an average position angle of ~ 77 – 83° (e.g., Harrison et al. 1986; Ulvestad et al. 1998; Mundell et al. 2003; Williams et al. 2017, see Fig. 2). Furthermore, we confirm with a higher confidence (detected at $\sim 3.5\sigma$ in the combined data versus $\sim 2.2\sigma$ in the individual observations) the change in polarization angle between the low energy bin (2 – 3.5 keV) and the higher bins (i.e., 3.5 – 5 keV and 5 – 8 keV)

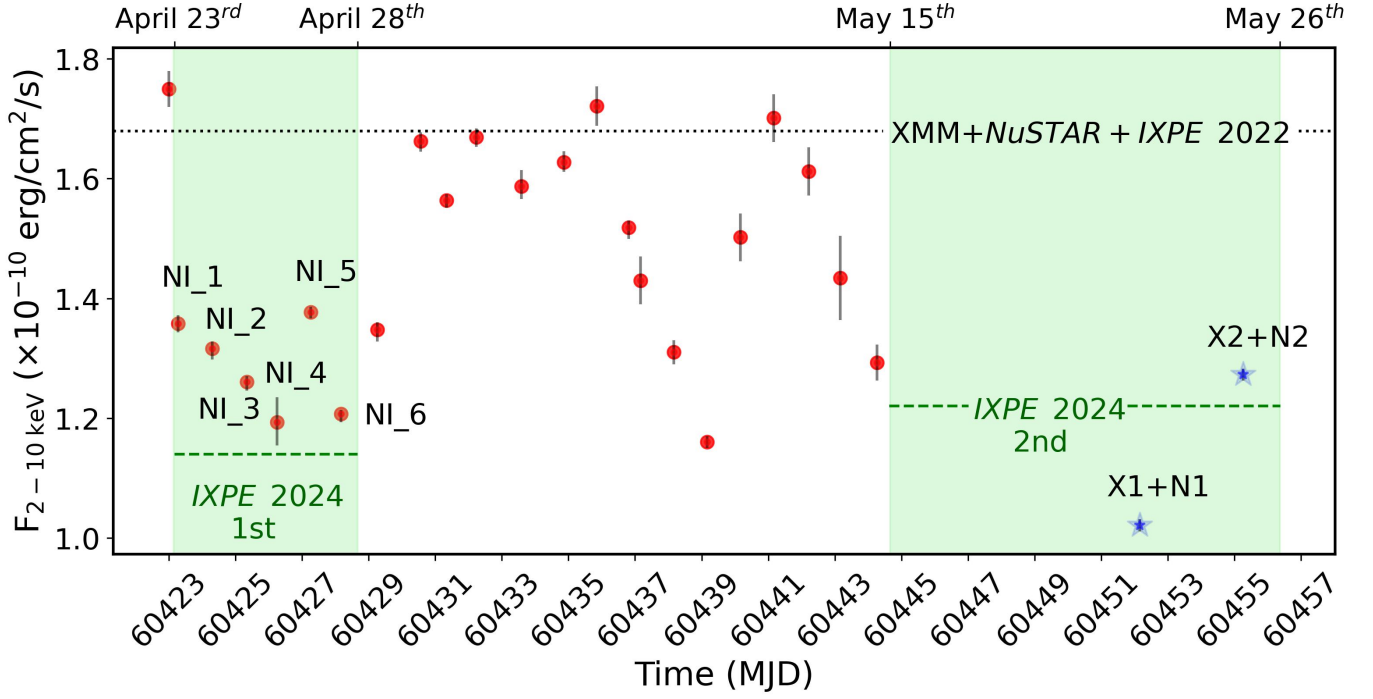


Fig. 5. Comparison between *NICER* XMM+*NuSTAR* flux. The observed flux for the *NICER* daily monitoring of NGC 4151 is shown in red dots. The light green bands show the two segments of the *IXPE* pointing and the dashed green lines are the respective extrapolated 2.0 – 10.0 keV fluxes. The blue stars are the flux values obtained for X1+N1 and X2+N2. The dotted black line represents the flux observed during the first observational campaign.

Table 3. Polarization degree and angle of each spectral component for different tests conducted during the spectro-polarimetric analysis.

Component	PD [%]	PA [°]	$\chi^2/\text{d.o.f}$
Model 1			
Primary continuum	7.1 ± 1.2	84 ± 5	
Soft emission	0^{fix}	–	1298/1222
Neutral reflection	<17	$PA_p \pm 90^\circ$	
Model 2			
Primary continuum	15.6 ± 2.3	99 ± 4	
Soft emission	13.1 ± 2.5	20 ± 6	1272/1221
Neutral reflection	0^{fix}	–	
Model 3A			
Primary continuum	19.4 ± 2.3	100 ± 4	
Soft emission	14.4 ± 2.5	20 ± 5	1276/1221
Neutral reflection	20^{fix}	$PA_p \pm 90^\circ$	
Model 3B			
Primary continuum	11.8 ± 2.5	98 ± 4	
Soft emission	11.8 ± 2.5	20 ± 6	1274/1221
Neutral reflection	20^{fix}	PA_p	
Model 4			
Primary continuum	7.0 ± 0.9	93 ± 4	
Soft emission	8.2 ± 2.2	22 ± 6	1287/1224
Neutral reflection	0^{fix}	–	

Notes. PA_p is the polarization angle of the primary continuum.

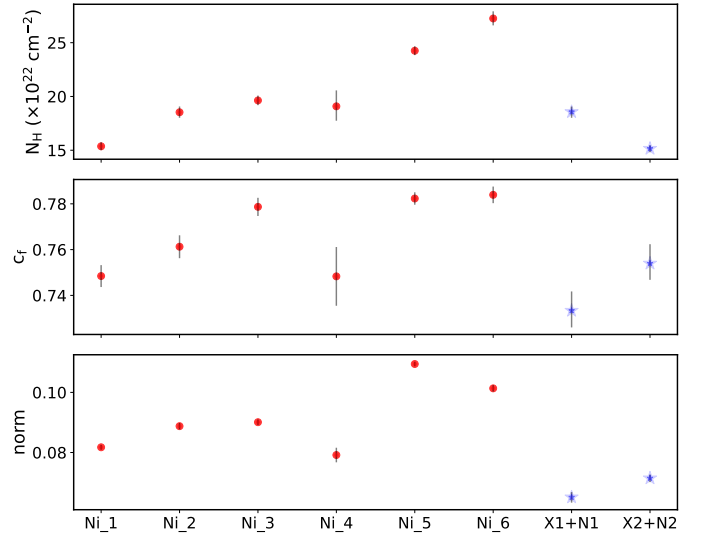


Fig. 6. Spectral parameters variability. We show the variations of the column density (upper panel) and covering factor (middle panel) of the first neutral partial covering, along with those of the primary continuum normalization (lower panel) for the *NICER* data (red dots) and for XMM+*NuSTAR* (blue stars).

or the full band, already observed in G23 (see Table 1 and Fig. 1 and 2). Interestingly, the PA in this soft X-ray bin (i.e., $37^\circ \pm 7^\circ$) appears to align with an unclassified feature identified by Draper et al. (1992) which presents an enhanced extra-nuclear polarization in *I*-band, located at $\sim 17''$ from the center at position angles of 35° and 215° (see Fig. 2).

A spectro-polarimetric fit on both *IXPE* observations give results in full agreement with what presented in G23, with more

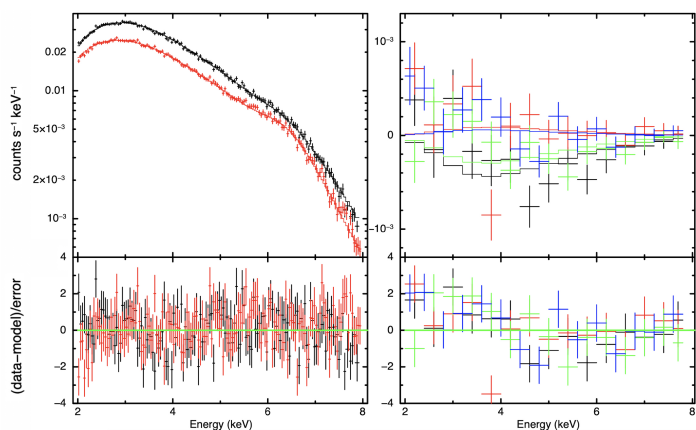


Fig. 7. *IXPE* spectra. *Left panel:* *IXPE* grouped Stokes *I* (in black the first and in red the second observation) spectra of NGC 4151 with residuals. *Right-panel:* *Q* (in black the first and in green the second observation) and *U* (in red the first and in blue the second observation) grouped Stokes spectra are shown with residuals.

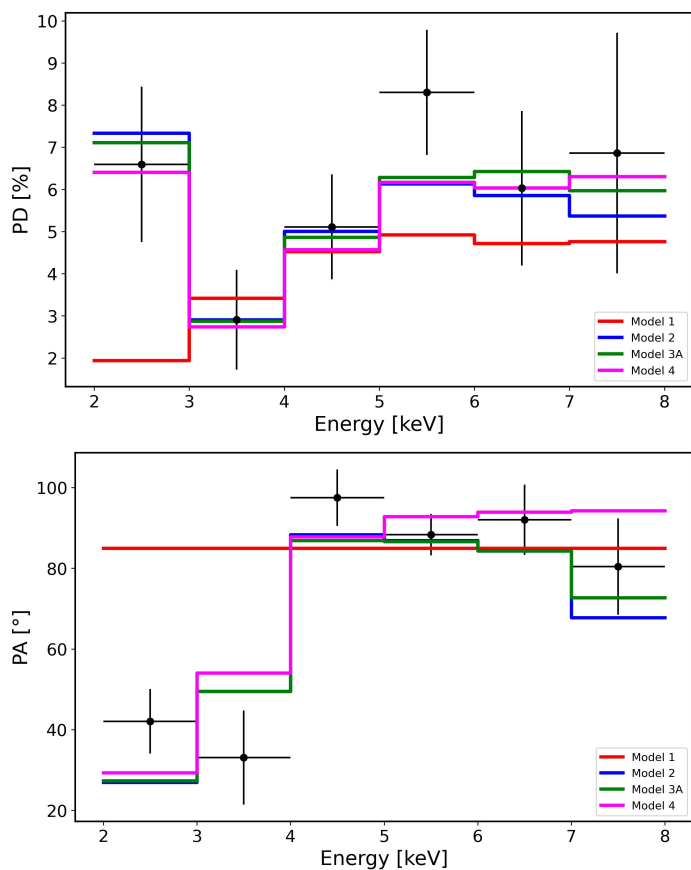


Fig. 8. Polarization properties as a function of energy. *Left panel:* polarization degree. *Right-panel:* polarization angle. Referring to the models presented in Table 3, we show Model 1 in red, Model 2 in blue, Model 3A in green, and Model 4 in magenta. The *IXPE* spectra are re-binned at interval of 1 keV.

constrained PD and PA values (i.e., $\Pi = 7.1 \pm 1.2$ per cent and $\Psi = 84^\circ \pm 5^\circ$) for the X-ray corona emission. As detailed in G23, these polarization properties are consistent with a slab or wedge geometry for the X-ray corona, as strongly reinforced by the alignment with the double-sided radio jet mentioned above.

However, in this spectro-polarimetric fit, an excess of the *Q* and *U* data with respect to the model is apparent below 4 keV

(see Fig. 7), driving the clear change of PA at lower energies (see Fig. 2 and 8). This observational evidence suggests the presence of an additional soft X-ray component, which could be dominated by the leakage of the primary emission through the absorbers, as modeled in our spectroscopic best-fit. We then allow the PA and PD of the leakage to vary, assuming that the reflection component is either unpolarized or has a PD of 20% with a PA parallel or perpendicular to the primary continuum (see Sect. 3.3). This improves the statistical quality of the spectro-polarimetric fit, notably modeling the PA switch at low energies (Table 3 and Fig. 8). The PD found for the soft component is fairly high (in the range 12-14 per cent), disfavoring the leakage hypothesis, rather suggesting scattering of the primary emission off the inner accretion flow or another mirror. In the latter case, this may suggest that the contribution of the NLR emission to the *IXPE* energy band is much larger than what predicted by our best-fit model, as a result of an over-simplification of the very complex spectrum of NGC 4151 around 2 keV. However, the PA attributed to this component in these spectro-polarimetric fits is around 20° , very distinct to the observed position angle of $\sim 60^\circ$ of the extended, biconical, NLR observed in near-IR, [O III] and X-rays (see e.g., Draper et al. 1992; Wang et al. 2011; Marin et al. 2020, and references therein).

These fits yield a higher PA for the primary continuum, around 100° , which somewhat departs from the position angle of the radio emission, although sub-arcsecond resolution observations have shown that the inner few pc of the radio jet is aligned with a position angle of $\sim 90^\circ$ (Mundell et al. 2003). Moreover, as for the soft X-ray component, the derived PD for the primary continuum is very high (10-20%), challenging the interpretation of this component as the intrinsic coronal emission. Both issues are solved by completely disentangling the primary continuum from the soft component thanks to a simplified phenomenological model, composed only by a power-law and a black-body. This suggests again that a significant part of the spectral complexity around 2-3 keV is not due to leakage of the primary continuum, but rather to an independent component.

We do not detect clear evidence of reflection off the accretion disk in the current data (see Sect. 3.2), nor in the 2022 spectra (see G23). However, we cannot rule out the possibility that a significant part of the X-ray polarization above ~ 4 keV is produced by disk reflection (see e.g., Podgorný et al. 2022, 2023), without clear spectroscopic signatures. This scenario will be explored with a self-consistent spectro-polarimetric analysis in a forthcoming publication (Dovčiak et al., in preparation). We note here that observing NGC 4151 with *IXPE* in a much lower flux state, could break this degeneracy and provide a more comprehensive understanding of the polarimetric properties of the AGN.

Acknowledgements. The Imaging X-ray Polarimetry Explorer (*IXPE*) is a joint US and Italian mission. The US contribution is supported by the National Aeronautics and Space Administration (NASA) and led and managed by its Marshall Space Flight Center (MSFC), with industry partner Ball Aerospace (contract NNM15AA18C). The Italian contribution is supported by the Italian Space Agency (Agenzia Spaziale Italiana, ASI) through contract ASI-OHBI-2017-12-I.0, agreements ASI-INAFA-2017-12-H0 and ASI-INFN-2017.13-H0, and its Space Science Data Center (SSDC) with agreements ASI-INAFA-2022-14-HH.0 and ASI-INFN 2021-43-HH.0, and by the Istituto Nazionale di Astrofisica (INAF) and the Istituto Nazionale di Fisica Nucleare (INFN) in Italy. This research used data products provided by the *IXPE* Team (MSFC, SSDC, INAF, and INFN) and distributed with additional software tools by the High-Energy Astrophysics Science Archive Research Center (HEASARC), at NASA Goddard Space Flight Center (GSFC). AT acknowledges financial support from the Bando Ricerca Fondamentale INAF 2022 Large Grant ‘Toward a holistic view of the Titans: multi-band observations of $z > 6$ QSOs powered by greedy supermassive black holes’. RS acknowledges funding from the INAF-PRIN grant ‘A Systematic Study of the largest reservoir of baryons and metals in the Uni-

verse: the circumgalactic medium of galaxies” (No. 1.05.01.85.10). We thank the *IXPE*, *NuSTAR*, *XMM-Newton*, and *NICER* SOCs for granting and performing the respective observations of the source.

Data Availability

The *IXPE* data used in this paper are publicly available in the HEASARC database (<https://heasarc.gsfc.nasa.gov/docs/ixpe/archive/>). The *XMM-Newton* and *NuSTAR* data underlying this article are subject to an embargo of 12 months from the date of the observations. Once the embargo expires (May 31, 2025) the data will be publicly available from the *XMM-Newton* science archive (<http://nxsas.esac.esa.int/>) and the *NuSTAR* archive (https://heasarc.gsfc.nasa.gov/docs/nustar/nustar_archive.html). The *NICER* data are publicly available in the HEASARC database (https://heasarc.gsfc.nasa.gov/docs/nicer/nicer_archive.html).

References

- Antonucci, R. R. J. & Cohen, R. D. 1983, *ApJ*, 271, 564
- Arnaud, K. A. 1996, in *ASP Conf. Ser.*, Vol. 101, *Astronomical Data Analysis Software and Systems V*, ed. G. H. Jacoby & J. Barnes (San Francisco: Astron. Soc. Pac.), 17–20
- Arzoumanian, Z., Gendreau, K. C., Baker, C. L., et al. 2014, in *Society of Photo-Optical Instrumentation Engineers (SPIE) Conference Series*, Vol. 9144, *Space Telescopes and Instrumentation 2014: Ultraviolet to Gamma Ray*, ed. T. Takahashi, J.-W. A. den Herder, & M. Bautz, 914420
- Baldini, L., Bucciantini, N., Lalla, N. D., et al. 2022, *SoftwareX*, 19, 101194
- Baloković, M., Brightman, M., Harrison, F. A., et al. 2018, *ApJ*, 854, 42
- Baloković, M., García, J. A., & Cabral, S. E. 2019, *Research Notes of the American Astronomical Society*, 3, 173
- Bentz, M. C., Williams, P. R., & Treu, T. 2022, *ApJ*, 934, 168
- Beuchert, T., Markowitz, A. G., Dauser, T., et al. 2017, *A&A*, 603, A50
- Bianchi, S., Chiaberge, M., Evans, D. A., et al. 2010, *MNRAS*, 405, 553
- De Rosa, A., Piro, L., Perola, G. C., et al. 2007, *A&A*, 463, 903
- Di Marco, A., Costa, E., Muleri, F., et al. 2022, *AJ*, 163, 170
- Di Marco, A., Soffitta, P., Costa, E., et al. 2023, *AJ*, 165, 143
- Draper, P. W., Gledhill, T. M., Scarrott, S. M., & Tadhunter, C. N. 1992, *MNRAS*, 257, 309
- Fabian, A. C., Lohfink, A., Belmont, R., Malzac, J., & Coppi, P. 2017, *MNRAS*, 467, 2566
- Fabian, A. C., Lohfink, A., Kara, E., et al. 2015, *MNRAS*, 451, 4375
- Ferland, G. J., Korista, K. T., Verner, D. A., et al. 1998, *PASP*, 110, 761
- Gendreau, K. C., Arzoumanian, Z., Adkins, P. W., et al. 2016, in *Society of Photo-Optical Instrumentation Engineers (SPIE) Conference Series*, Vol. 9905, *Space Telescopes and Instrumentation 2016: Ultraviolet to Gamma Ray*, ed. J.-W. A. den Herder, T. Takahashi, & M. Bautz, 99051H
- Gendreau, K. C., Arzoumanian, Z., & Okajima, T. 2012, in *Society of Photo-Optical Instrumentation Engineers (SPIE) Conference Series*, Vol. 8443, *Space Telescopes and Instrumentation 2012: Ultraviolet to Gamma Ray*, ed. T. Takahashi, S. S. Murray, & J.-W. A. den Herder, 844313
- Gianolli, V. E., Bianchi, S., Petrucci, P.-O., et al. 2024, in *Memorie della Società Astronomica Italiana*, Vol. 95, 27–31
- Gianolli, V. E., Kim, D. E., Bianchi, S., et al. 2023, *MNRAS*, 523, 4468
- Harrison, B., Pedlar, A., Unger, S. W., et al. 1986, *MNRAS*, 218, 775
- Harrison, F. A., Craig, W. W., Christensen, F. E., et al. 2013, *ApJ*, 770, 103
- Ingram, A., Ewing, M., Marinucci, A., et al. 2023, *MNRAS*, 525, 5437
- Kaastra, J. S. & Bleeker, J. A. M. 2016, *A&A*, 587, A151
- Kamraj, N., Brightman, M., Harrison, F. A., et al. 2022, *ApJ*, 927, 42
- Kang, J.-L. & Wang, J.-X. 2022, *ApJ*, 929, 141
- Keck, M. L., Brenneman, L. W., Ballantyne, D. R., et al. 2015, *ApJ*, 806, 149
- Kraemer, S. B., Schmitt, H. R., & Crenshaw, D. M. 2008, *ApJ*, 679, 1128
- Lubiński, P., Zdziarski, A. A., Walter, R., et al. 2010, *MNRAS*, 408, 1851
- Marin, F., Gianolli, V. E., Ingram, A., et al. 2024, *Galaxies*, 12
- Marin, F., Le Cam, J., Lopez-Rodríguez, E., et al. 2020, *MNRAS*, 496, 215
- Marinucci, A., Muleri, F., Dovciak, M., et al. 2022, *MNRAS*, 516, 5907
- Matt, G., Baloković, M., Marinucci, A., et al. 2015, *MNRAS*, 447, 3029
- May, D., Steiner, J. E., Menezes, R. B., Williams, D. R. A., & Wang, J. 2020, *MNRAS*, 496, 1488
- Muleri, F. 2022, *Analysis of the Data from Photoelectric Gas Polarimeters*, ed. C. Bambi & A. Santangelo (Singapore: Springer Nature Singapore), 1–23
- Mundell, C. G., Wrobel, J. M., Pedlar, A., & Gallimore, J. F. 2003, *ApJ*, 583, 192
- NASA Heasarc. 2014, *HEASoft: Unified Release of FTOOLS and XANADU*, *Astrophysics Source Code Library*, record ascl:1408.004
- Petrucci, P. O., Haardt, F., Maraschi, L., et al. 2001, *ApJ*, 556, 716
- Piconcelli, E., Jimenez-Bailón, E., Guainazzi, M., et al. 2004, *MNRAS*, 351, 161
- Podgorný, J., Dovciak, M., Goosmann, R., et al. 2023, *MNRAS*, 524, 3853
- Podgorný, J., Dovciak, M., Marin, F., Goosmann, R., & Różańska, A. 2022, *MNRAS*, 510, 4723
- Ricci, C., Ho, L. C., Fabian, A. C., et al. 2018, *MNRAS*, 480, 1819
- Schnittman, J. D. & Krolik, J. H. 2010, *ApJ*, 712, 908
- Serafinelli, R., De Rosa, A., Tortosa, A., et al. 2024, *arXiv e-prints*, arXiv:2407.06769
- Serafinelli, R., Marinucci, A., De Rosa, A., et al. 2023, *MNRAS*, 526, 3540
- Shapiro, S. L., Lightman, A. P., & Eardley, D. M. 1976, *ApJ*, 204, 187
- Shapovalova, A. I., Popovic, L. C., Collin, S., et al. 2012, *Astron. Astrophys. Trans.*, 27, 429
- Storch-Bergmann, T., McGregor, P. J., Riffel, R. A., et al. 2009, *MNRAS*, 394, 1148
- Strüder, L., Briel, U., Dennerl, K., et al. 2001, *A&A*, 365, L18
- Sunyaev, R. A. & Titarchuk, L. G. 1980, *A&A*, 86, 121
- Tagliacozzo, D., Marinucci, A., Ursini, F., et al. 2023, *MNRAS*, 525, 4735
- Tamborra, F., Matt, G., Bianchi, S., & Dovciak, M. 2018, *A&A*, 619, A105
- Tortosa, A., Bianchi, S., Marinucci, A., Matt, G., & Petrucci, P. O. 2018, *A&A*, 614, A37
- Ulvestad, J. S., Roy, A. L., Colbert, E. J. M., & Wilson, A. S. 1998, *ApJ*, 496, 196
- Ursini, F., Matt, G., Bianchi, S., et al. 2022, *MNRAS*, 510, 3674
- Wang, J., Fabbiano, G., Risaliti, G., et al. 2011, *ApJ*, 729, 75
- Weaver, K. A., Mushotzky, R. F., Arnaud, K. A., et al. 1994, *ApJ*, 423, 621
- Weisskopf, M. C., Soffitta, P., Baldini, L., et al. 2022, *J. Astron. Telesc. Instrum. Syst.*, 8, 026002
- Williams, D. R. A., McHardy, I. M., Baldi, R. D., et al. 2017, *MNRAS*, 472, 3842
- Wolfinger, K., Kilborn, V. A., Koribalski, B. S., et al. 2013, *MNRAS*, 428, 1790
- Yang, Y., Wilson, A. S., & Ferruit, P. 2001, *ApJ*, 563, 124
- Yaqoob, T., Edelson, R., Weaver, K. A., et al. 1995, *ApJ*, 453, L81
- Zdziarski, A. A., Johnson, W. N., & Magdziarz, P. 1996, *MNRAS*, 283, 193
- Zdziarski, A. A., Poutanen, J., & Johnson, W. N. 2000, *ApJ*, 542, 703
- Zhang, W., Dovciak, M., & Bursa, M. 2019, *ApJ*, 875, 148
- Zoghbi, A., Miller, J. M., & Cackett, E. 2019, *ApJ*, 884, 26
- Życki, P. T., Done, C., & Smith, D. A. 1999, *MNRAS*, 309, 561

Affiliations:

- ¹Université Grenoble Alpes, CNRS, IPAG, 38000 Grenoble, France
- ²Dipartimento di Matematica e Fisica, Università degli Studi Roma Tre, Via della Vasca Navale 84, 00146 Roma, Italy
- ³ASI - Agenzia Spaziale Italiana, Via del Politecnico snc, 00133 Roma, Italy
- ⁴INAF – Astronomical Observatory of Rome, Via Frascati 33, 00040 Monte Porzio Catone, Italy
- ⁵INAF Istituto di Astrofisica e Planetologia Spaziali, Via del Fosso del Cavaliere 100, I-00133 Roma, Italy
- ⁶Dipartimento di Fisica, Università degli Studi di Roma “La Sapienza”, Piazzale Aldo Moro 5, I-00185 Roma, Italy
- ⁷Dipartimento di Fisica, Università degli Studi di Roma “Tor Vergata”, Via della Ricerca Scientifica 1, I-00133 Roma, Italy
- ⁸Université de Strasbourg, CNRS, Observatoire Astronomique de Strasbourg, UMR 7550, 67000 Strasbourg, France
- ⁹Centre for Extragalactic Astronomy, Department of Physics, University of Durham, South Road, Durham DH1 3LE, UK
- ¹⁰Institute of Space and Astronautical Science (ISAS), Japan Aerospace Exploration Agency (JAXA), Kanagawa 252-5210, Japan
- ¹¹MIT Kavli Institute for Astrophysics and Space Research, Massachusetts Institute of Technology, 77 Massachusetts Avenue, Cambridge, MA 02139, USA
- ¹²Space Science Data Center, Agenzia Spaziale Italiana, Via del Politecnico snc, 00133 Roma, Italy

¹³*Astronomical Institute of the Czech Academy of Sciences,
Bocřní II 1401/1, 14100 Praha 4, Czech Republic*

¹⁴*Istituto Nazionale di Fisica Nucleare, Sezione di Roma "Tor
Vergata", Via della Ricerca Scientifica 1, 00133 Roma, Italy*

¹⁵*Department of Astronomy, University of Maryland, College
Park, Maryland 20742, USA*